Supporting Information

Silicon Acid Batteries Enabled by a Copper Catalysed Electrochemo-Mechanical Coupled Process

Yaquan Tao [a], Qiyuan Zhou [a], Chengjie Cai [a], Chunyuan Song [a], Hai Li [b], Xiao Huang [b], Lijun Yang [c], Wei Huang [a,b,d]*, Shaozhou Li [a]*

a.   Institute of Advanced Materials, Nanjing University of Posts & Telecommunications, Wenyuan Road, Nanjing 210023, P.R. China
b.   Institute of Advanced Materials (IAM), Nanjing Tech University (NanjingTech), 30 South Puzhu Road, Nanjing 211816, P.R. China.
c.   Key Laboratory of Mesoscopic Chemistry of MOE and Jiangsu Provincial Lab for Nanotechnology, School of Chemistry and Chemical Engineering, Nanjing University, Nanjing, 210023 China
d.   Shaanxi Institute of Flexible Electronics (SIFE), Northwestern Polytechnical University (NPU), 127 West Youyi Road, Xi'an 710072, Shaanxi, China.

Methods and Experimental Notes:

The synthesis procedure

0.2 g silicon particles were dispersed in a solution of polyvinylpyrrolidone (PVP, 5g, M_w=55000) in DI water (200 mL) and the mixture was further stirred for 24 h. The PVP coated silicon particles were collected by centrifugation and washed with methanol 3 times before redispersed in 200 mL methanol. The PVP coated silicon particles were then mixed with 200 mL methanol solution of $Zn(NO)_3·6H_2O$ (50 mM) and 200 mL methanol solution of 2-methylimidazole (50 mM). The mixture was shaken at room temperature for 24 h. The product was collected by centrifugation, washed 4 times with methanol and vacuum-dried overnight before 2mL methanol solution of $CuCl_2$ (containing 40 mg dehydrated $CuCl_2$) was added. The product was dried in oven before heat treatment in N_2 at 900 °C for 3 h. The product was washed by diluted HNO_3 and HF solution separately to remove element copper and silicon dioxide before further characterizations. For comparison, carbon coated silicon particles were also prepared through the heat treatment of MOF coated silicon particles prepared by the same method in N_2 at 900 °C for 3 h, which is denoted as Si@C. Furthermore, the dehydrated $CuCl_2$ was replaced with $FeCl_2$ (40 mg) and $NiCl_2$ (40 mg) to synthesis the iron and nickel deposited silicon particles, respectively.

α-MnO_2 nanorods were prepared by a hydrothermal method. In a typical experiment, 5 mM $KMnO_4$ was first dissolved into the solution of 24 ml of 1 M HCl. Then, the volume was filled to 70 ml by adding DI water. After stirring for half an hour, the solution was transferred into a 250-ml autoclave. The autoclave was placed at 140°C and reacted for 18 hours. The solution was then filtered to obtain the solid product, which was washed by DI water and ethanol for four times. The product was dried in vacuum oven at 80°C.

Material characterizations

XRD (Bruker Advanced D8) was performed with Cu Kα radiation (λ=1.54 Å) as the X-ray source. Scanning electron microscopy (SEM, Hitachi S-4800) was used for the morphology analysis. To gain the crystal structure information, high-resolution transmission electron

microscopy (HRTEM, JEOL 2100F) coupled with energy dispersive X-ray spectroscopy (EDS) analyses were performed. The STEM characterization was carried out on a JEOL ARM-200F (S)TEM equipped with CEOS CESCOR aberration corrector. The sample for STEM characterization was prepared by focused ion beam (FIB, JIB-4000PLUS). The chemical state study of the samples was carried out by XPS (PHI 5000 VersaProbe) and the binding energies were corrected for specimen charging effects using the C 1s level at 284.6 eV as the reference. The lineshapes used for XPS curve fitting were pure Gaussian and integrated backgrounds were employed.

Electrochemical measurements

The measurements were carried out in acid electrolyte (1mol/kg H_2SO_4 + 2mol/kg Na_2SO_4) where Na_2SO_4 was employed to enhance the conductivity of the electrolyte. The active material was coated on carbon cloth electrode. In galvanostatic discharge measurements, Si@C and Cu-Si@C electrodes were used as the counter and reference electrodes with platinum wire as the working electrode in CHI 660e at the selected current density. The EIS measurements were carried out on an electrochemical station (Autolab 302N) at OCP condition in the frequency range of $0.01-10^4$ Hz with an AC perturbation of 5 mV in amplitude. Polarization curves were generated using a CHI 660e. The voltage was measured while the current was scanned at $1mA/cm^2$ per minute intervals. Measurements were carried out after the electrolyte filled the electrode gaps of the cell for 3 min. All the silicon acid batteries were fabricated in atmospheric environment. To prepare Si@C anode, Si@C particles, super P, and polyvinylidene fluoride (PvdF) with a weight ratio of 70:20:10 were mixed with N-methylpyrone (NMP) and painted on carbon fiber paper. The anode was obtained after removing NMP at 80°C overnight. The areal loading of Si@C is about 1 mg/cm^2. The Cu-Si@C anode was prepared by mixing Cu-Si@C, super P and PvdF with a weight ratio of 80:10:10 in NMP and the slurry was painted on carbon fiber paper before baking at 80°C overnight. The areal loading of Cu-Si@C is about 1.1 mg/cm^2. To prepare MnO_2 cathode, MnO_2, super P, and PvdF with a weight ratio of 70:20:10 were mixed with NMP and painted on carbon fiber paper. The cathode was obtained after removing NMP at 80°C overnight. The areal loading of MnO_2 is about 2 mg/cm^2 and the mass ratio of Cu-Si@C:MnO_2 in the assembled batteries was set at ~1:10. For the air cathode preparation, a carbon fiber paper deposited with 20 wt.% Pt-C (~1 mg/cm^2) was used. All the battery tests were measured by CHI 660e in a thermostatic chamber at 60 °C.

Simulations

The density functional theory (DFT) calculation has been carried out by using the plane-wave code CASTEP [1]. The Perdew, Bruker, and Ernzerhof (PBE) generalized gradient approximation (GGA) was used for the exchange-correction potential. A kinetic energy cutoff of 600 eV was set and the Monkhorst-Pack scheme to generate the k-space grid using a spacing of 0.1 $Å^{-1}$. A SiO_2/Si interface model was built with a (2×2) Si supercell connected with bridge-oxygen to one monolayer of silicon oxide. During geometric optimization, the bottom 5 layer slabs were fixed at a bulk truncated position. For all of the calculation, the vacuum slab region is 15 Å.

The EIS analysis

Attributed to the growth of dense and continuous SiO_2 layer which quenches the electrochemical reaction, an almost zero current on the Si@C electrode was obtained under steady state. Thus the EIS of Si@C electrode shows a blocking electrode behavior in which the semicircle was not presented at the high frequency region of the Nyquist plot and no peak of phase angle were shown on its Bode plot (Fig. S6 and Fig. 3b). In contrast, a reaction process was shown for Cu-Si@C electrode and the peak of phase angle at ~ 0.1 Hz was presented (Fig.

3b). Under the charge-transfer controlled electrode reaction, the frequency for the maximum phase angle can be estimated as follows:

$$\omega(\alpha_{max}) = \frac{\sqrt{1+(^{R_{ct}}/_{R_s})}}{R_{ct}C_{dll}} \qquad (1)$$

In which ω stands for the radical frequency and can be converted to frequency by the equation $\omega=2\pi f$, α_{max} is the maximum phase angle, R_s is the solution resistance, R_{ct} is the charge transfer resistance and C_{dll} is the double layer capacity of the electrode. The electrochemical fitting of the Nyquist plot in Fig. 3b shows that R_s is 1.41Ω and R_{ct} is $876.19\ \Omega$ for the discharged Cu-Si@C electrode. The double-layer capacitance (C_{dll}) of the CuSi@C after discharge can be estimated from its CV measurement in a potential range of 0.5-0.6 V vs. Hg/Hg_2SO_4 where no apparent faradaic processes occurred under different scan rates (Fig. S7) and a very large capacity of 74.63 mF/cm^2 was achieved. For a comparison, the C_{dll} of a standard smooth metal oxide electrode is $\sim 60\ \mu F/cm^2$. Thus the shift of the peak to much smaller region than conventional electrodes (100~1000 Hz) is attributed to the increased electrode capacitance. the ω (α_{max}) of the Cu-Si@C electrode is about three orders smaller than typical electrodes and the characteristic frequency for maximum phase angle can be estimated ~0.061 Hz, which is in line with the result obtained from the Bode plot (Fig. 3b).

The kinematics of fracture growth of the electrochemical oxidized silicon particle
Assuming the Si particle is spherical and oxidation can induce large deformation of the structure (Fig. S18). The kinematics study of the oxidized particle was carried out using a model similar with the strained lithiated silicon electrode [2].

The diffusivity of H_2O in SiO_2 at room temperature is 10^{-15}~10^{-16} cm^2/s from the extrapolation of the result obtained by Tomozawa et al.[3], which is consistent with the result obtained by Landford et al. at 90°C [4]. Therefore, the growth velocity of SiO_2 should be 10^{-7}~10^{-8} cm/s, which is much larger than the reported oxidation velocity of silicon in pure water ($\sim 1.2\times10^{-14}$ cm/s) [5]. Therefore, the reaction of Si with water is more likely limited by the rate of the reaction between Si and H_2O at interface at room temperature.

The kinematics of the large deformation of the particle is specified as follows. The spherical particle consists of a field of element silicon. The element silicon along the distance of R from the center in the initial state moves to a place along distance r from the center at time t. Thus a Si/SiO_2 core-shell structure forms with the radius of the crystalline core being A, and the outer radius of the amorphous shell being b. The function A(t) specifies the extent of reaction and the velocity of the reaction front is $V = -dA(t)/dt$. During reaction, the initial radius of the silicon particle is R. At time t, the element on R moves to a place of radius r. The function r (R, t) specifies the formation of the particle. Because elastic strain is much smaller than the volumetric strain associated with the phase transition for Si to SiO_2, we thus neglect elastic strains of both phases and model the crystalline silicon as one rigid material, and SiO_2 as one rigid-plastic material for simplification. Consequently, the expansion of the particle is entirely due to the oxidation.

Considering the SiO_2 shell between the radii A and r, it is oxidized from the shell of the pristine crystalline Si between the radii A and R. The ratio of the volume of the SiO_2 shell over the volume of the crystalline shell is β, so that $r^3 - A^3 = \beta(R^3 - A^3)$. Therefore, the outer radius of the particle is $b = [A^3 + \beta(B^3 - A^3)]$.

3

The normal stretch is $\lambda_r = \dfrac{\partial r(R,t)}{\partial R}$ (2)

The hydrostatic stretch is $\lambda_\theta = \dfrac{r}{R}$ (3)

Let σ_r the normal stress and σ_θ the hydrostatic stress. For simplicity, we set $|\sigma_\theta - \sigma_r| = \sigma_b$, where σ_b is the tensile strength. The balance of forces requires that

$$\frac{\partial \sigma_r(R,t)}{\lambda_r \partial R} + 2\frac{\sigma_r - \sigma_\theta}{\lambda_\theta R} = 0$$ (4)

Integrating the traction-free boundary condition $\sigma_r(b,t) = 0$ over r and $\sigma_r - \sigma_\theta = \sigma_b$, the normal stress in the shell is obtained

$$\sigma_r = -2\sigma_b \log\left(\frac{b}{r}\right), \ A \le r \le b$$ (5)

The hydrostatic stress inside the SiO_2 shell away from the interface is

$$\sigma_\theta = \sigma_b - 2\sigma_b \log\left(\frac{b}{r}\right), \ A \le r \le b$$ (6)

Near the SiO_2/Si interface, the silicon lattice from crystalline silicon undergoes tensile plastic deformation in the directions tangential to the interface. Therefore, the hydrostatic stress of silicon is determined from $\sigma_r - \sigma_\theta = -\sigma_b$, giving

$$\sigma_\theta = -\sigma_b - 2\sigma_b \log\left(\frac{b}{A}\right), \ r = A$$ (7)

We then consider the retardation of the reaction by the strain field. The work has been done by the stress pushing the oxidized unit away from the interface. Therefore, one Si atom has to do work ΔW to overcome the strain effect and which can be written as:

$$\Delta W = \sigma^{Si}\Omega^{Si} - \sigma^{SiO_2}\Omega^{SiO_2}$$ (8)

Where Ω is the volume per atom/cluster in the material, σ is the stress and here we use mean stress σ_m in Si and SiO_2 at the interface for simplification.

Thus, $\sigma_m^{Si} = -2\sigma_b \log\left(\frac{b}{A}\right) and \ \sigma_m^{SiO_2} = -2\sigma_b \log\left(\frac{b}{A}\right) - \frac{2\sigma_b}{3}$

As $\beta = \dfrac{\Omega^{SiO_2}}{\Omega^{Si}}$, the equation (8) can be rewritten as

$$\Delta W = 2\sigma_b\Omega^{Si}\left[(\beta - 1)\log\left(\frac{b}{A}\right) + \beta/3\right]$$ (9)

For SiO_2, the represented value of σ_b is 1.6 GPa. We assume the initial radii of the Si particle is 100 nm. The hydrostatic stress at SiO_2/Si interface and the work need to be overcome with oxidation proceeded was calculated and plotted in Fig. S19.

The corrosion investigation of Cu-Si@C

The direct measurement of corrosion rate for Cu-Si@C in contact with the electrolyte is difficult. We have tried to estimate corrosion rate of the silicon wafer with copper dopant using the mass-loss method. However, no visible weight change was record when the standard error

is considered. Therefore, the chemical and electrochemical corrosion rate of the anode was estimated based on the electrochemical measurement results. We monitored the discharge of one Cu-Si@C/MnO$_2$ cell under different conditions (Fig. S28). For day 1, day 2, day 3, day 4, day 5 and day 12, the cell was discharged at 0.1 mA/cm^2 for 0.5 h each interval. The output voltage dropped fast at day 4. Once the Cu-Si@C electrode was washed with diluted HF solution (5 wt.%) to remove the surface oxide, the recovery of the output voltage was observed. If the cell was stored in vacuum condition and the dissolved oxygen in the electrolyte was removed before further discharge, the output voltage remains even after one week. Therefore, it seems the chemical corrosion of Cu-Si@C electrode in acid solution is mainly resulted from the electrode oxidation by the dissolved oxygen in the solution.

Furthermore, experiment on the electrode used in Fig. S28 was carried out (Fig. S29). The battery was discharged at 0.1 mA/cm^2 in air before O$_2$ gas was injected by one syringe. The output voltage dropped immediately. Then, 0.2 mL H$_2$O$_2$ was added when the voltage is stable. The voltage dropped down continuously with the slow release of O$_2$ by H$_2$O$_2$ decomposition. Therefore, the chemical corrosion of silicon induces the formation of continuous SiO$_2$ layer which can block further reaction of silicon with the electrolyte and thus suppresses the further chemical corrosion of Cu-Si@C electrode. The chemical corrosion rate can be estimated as follows: As the Cu-Si@C loading on the electrode is ~1.1 mg/cm^2, it can be normalized to the thickness of silicon at ~4.4 µm. As the electrode has been immersed in electrolyte solution for one week in vacuum conditions before further discharge, the chemical corrosion rate should be smaller than 0.02 µm/h, which is two orders smaller than the corrosion rate of silicon in 6 M KOH solution (~1.5µm/h). Thus the corrosion of Cu-Si@C in the acid solution is more than two orders slower than it in the alkaline solution.

The electrochemical corrosion of Cu-Si@C electrode was estimated by the polarization resistance method and a corrosion current of ~10^{-5} mA/cm^2 was achieved (Fig. S30), which is about 3 orders smaller than that in KOH solution [6].

Specific capacity estimation of the full cells

The combination of single reaction on anode and cathode is defined as total reaction here. Therefore, the theoretical specific capacity of a full battery cell based on the total reaction can be estimated as follows:[16]

$$C_s^{th} = \frac{nF}{M} \tag{10}$$

Where C_s^{th} is the calculated capacity base on total reaction, n is the electron number of the electrode reactions; F equals to 26.8 Ah; M is the relative molecule weight of all the electroactive components (anode, cathode and electrolyte) based on the battery reaction equation (Table S2).

For Si-MnO$_2$ battery, the electrochemical reduction of MnO$_2$ involves a three-step reaction [7], which is (1) MnO$_2$+H$^+$+e→MnOOH; (2) MnOOH+3H$^+$→Mn^{3+}+2H$_2$O; (3) Mn^{3+}+e→Mn^{2+}. Therefore, we use Mn^{2+} as the reaction product and the total reaction is simplified as follows:

$$Si + MnO_2 \rightarrow SiO_2 + Mn^{2+} + 2e$$

The theoretical specific capacity is estimated as follows:

$$C_s^{th}(Si-MnO_2) = \frac{4 \times 26.8}{28+87} = \frac{0.932 Ah}{kg} = 932 \; mA \; h/g$$

For Si-air battery, the total reaction is:

$$Si + O_2 \rightarrow SiO_2$$
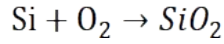
The theoretical specific capacity is estimated as follows:

$$C_s^{th}(Si-air) = \frac{4 \times 26.8}{28+18} = \frac{2.331 Ah}{kg} = 2331 \; mA \; h/g$$

The same method has been used to estimate the capacities of other primary batteries and the results are listed on Supplementary Table 2.

The electrolyte consumption during the cell reaction

A typical electrochemical cell for long-time durability test is made by Cu-Si@C anode (2cm×2cm, ~4.5 mg active material), MnO_2 cathode (4cm×8cm, ~80 mg active material) and electrolyte (1 mL Na_2SO_4+H_2SO_4 solution). Extra amount of electrolyte is needed at beginning because the solution can be adsorbed by the carbon cloth collector and each time anode exchange will lose 0.15~0.2 g solution from the cell. After the test, the net weight lost (the weight of initial cell plus the weight of extra anode electrodes before use minus the weight of finial cell and the weight of anode electrodes after use) is about 10 mg. This difference maybe mainly result from vaporization of the liquid solution during the cell reaction since it works at 60 °C and with simple mechanical seal. For a comparison, an electrolyte flow is needed to maintain the long run discharge for the silicon alkaline batteries (ref. 26). Therefore, the electrolyte consumption in the silicon acid cell is much reduced.
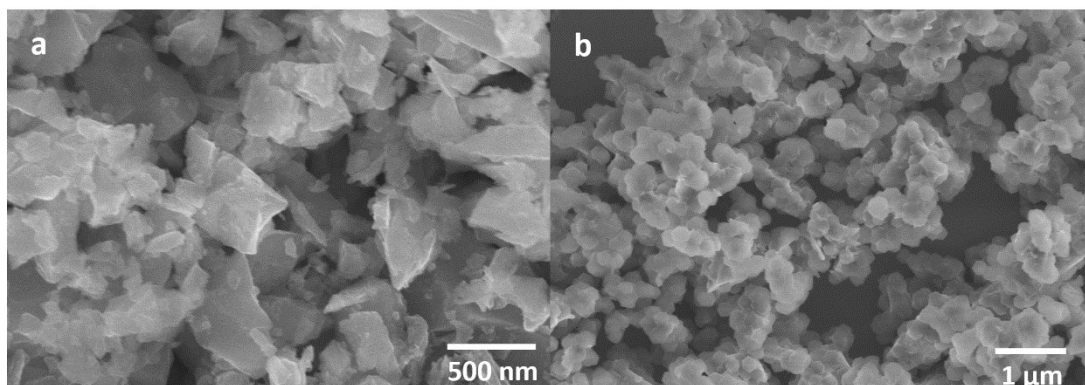
Figure S1. SEM images of (**a**) the as prepared silicon particles, and (**b**) the silicon particles coated with ZIF-8 layer.
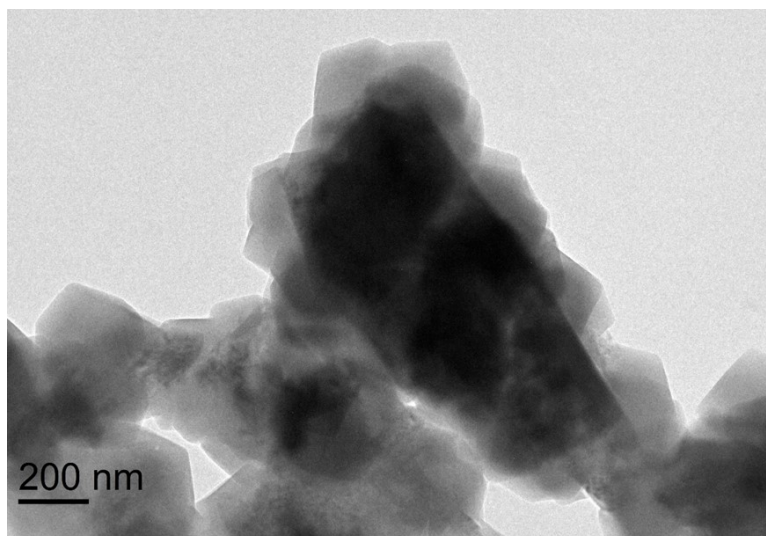
Figure S2. TEM image of the ZIF-8 coated silicon particles.
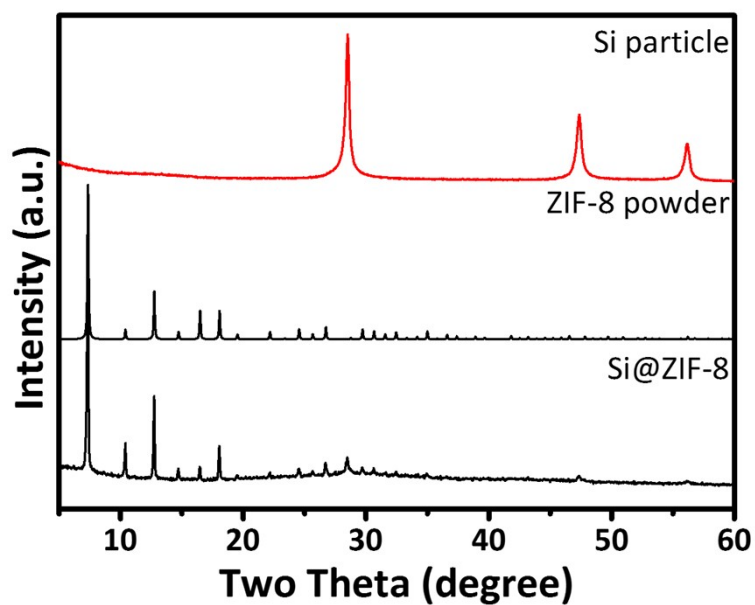
Figure S3. XRD patterns of the silicon particles, the simulated ZIF-8 powder and the Si@MOF (ZIF-8) particles.
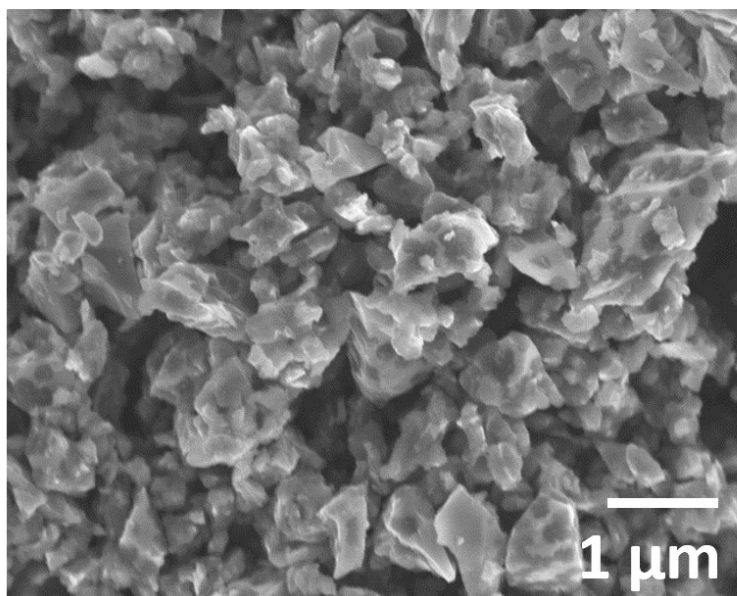
Figure S4. SEM image of the Cu-Si@C particles.

Element	Weight%	Atomic%
C K	26.94	41.38
O K	24.56	28.32
Si K	44.24	29.06
Cu K	4.26	1.24
Totals	100.00	

Full Scale 753 cts Cursor: 0.000
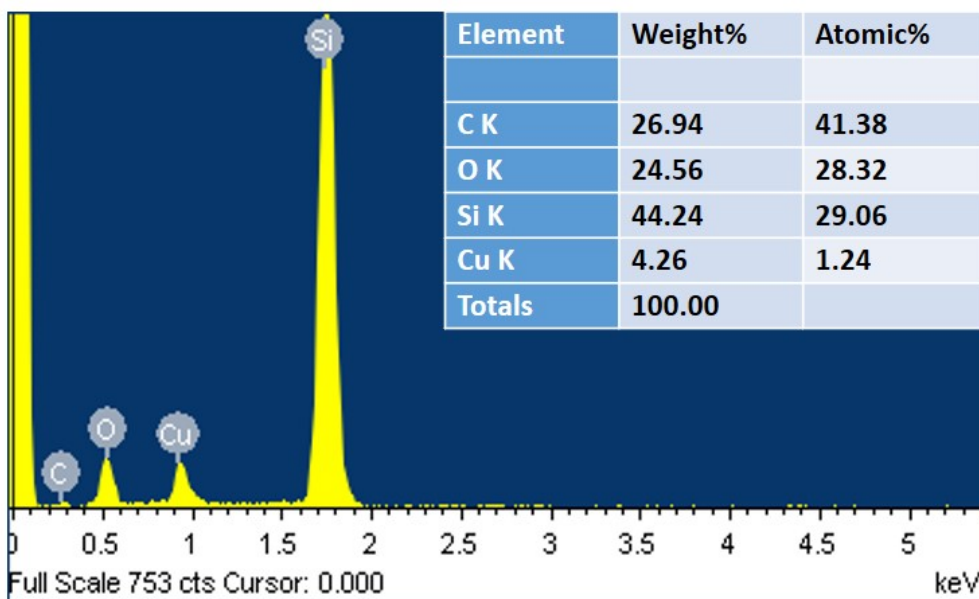
Figure S5. EDS spectrum of the as prepared Cu-Si@C powder. The Cu to Si atomic ratio is ~1:23.
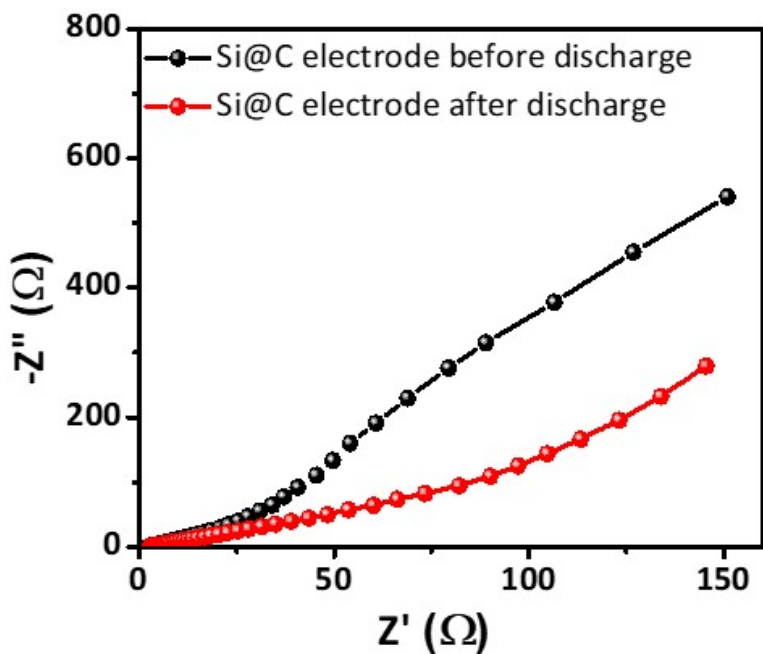
Figure S6. Nyquist plots of the Si@C electrode before and after discharge.
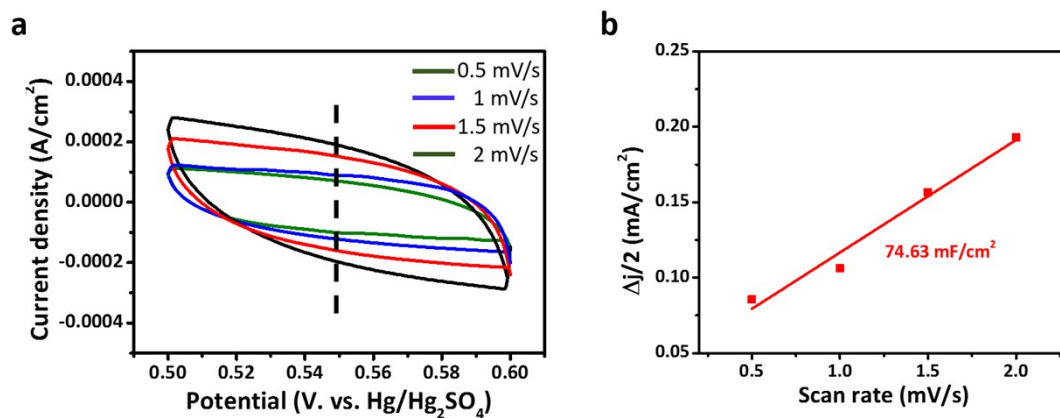
Figure S7. (**a**) Current density difference at 0.55 V (vs. Hg/Hg$_2$SO$_4$) plotted against scan rate to give (**b**) the double-layer capacitance (C$_{dll}$) for the Cu-Si@C electrode after discharge.
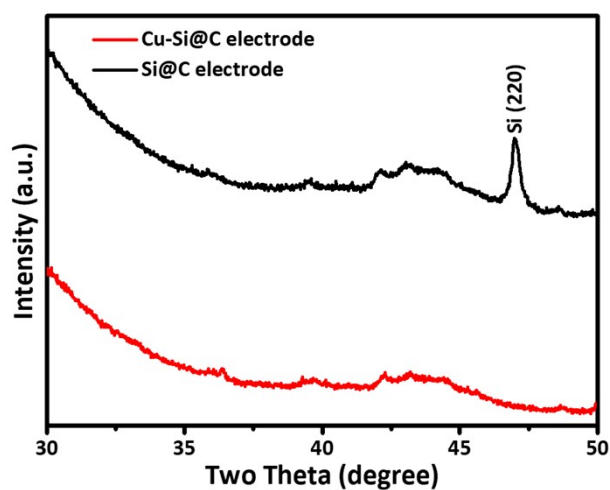
Figure S8. XRD for the Si@C electrode and Cu-Si@C electrode after complete discharge when paired with Pt mesh as the cathode.
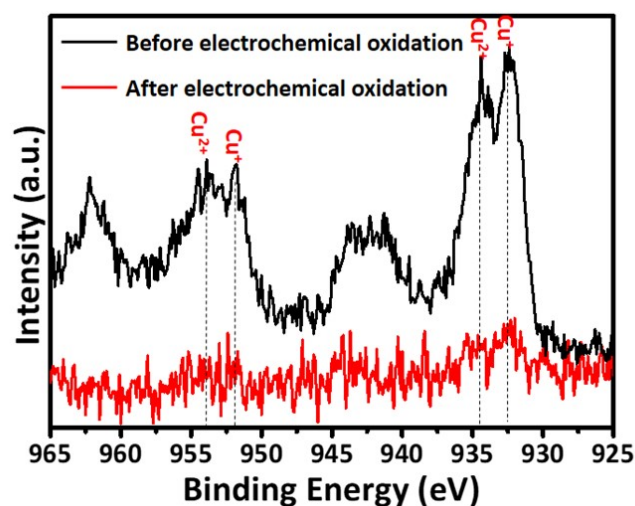
Figure S9. XPS Cu 2p of the Cu-Si@C electrode before and after electrochemical oxidation. The peaks intensity is dramatically decreased owing to the dissolution of element Cu into the electrolyte solution.
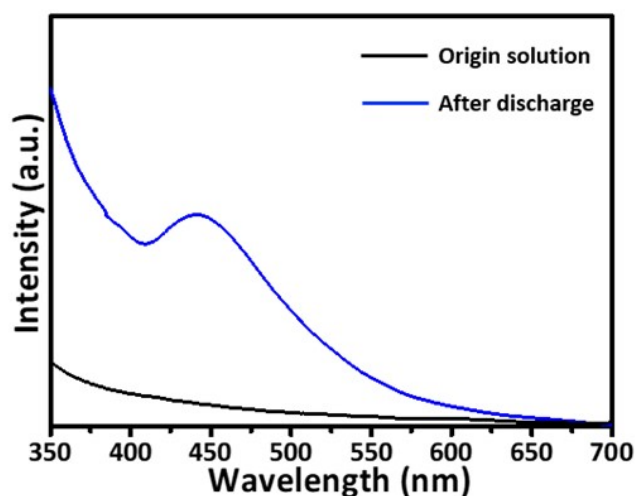
Figure S10. UV-vis absorption spectra of the origin H_2SO_4+$NaSO_4$ solution and the solution after electrochemical reaction (to detect the presence of copper ion, the pH of the solution was tuned to ~8 by NaOH and sodium dithiocarb was added). Due to the complexation of copper ion with sodium dithiocarb, a characteristic peak at ~450 nm was shown in the UV-vis aborption spectrum of the solution after discharge.
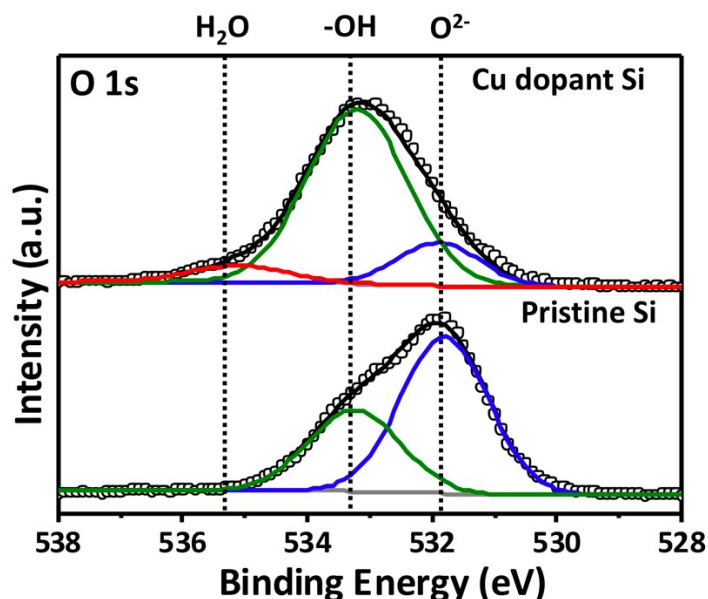
Figure S11. XPS O 1s of the pristine silicon wafer and the silicon wafer with Cu dopant after discharge for 1 h at a current density of 0.1 mA/cm^2.

To exclude the influence of oxygen in the carbon cages, silicon wafer rather than CuSi@C was used as the electrode. The copper doped silicon wafer was prepared by heat treatment of the silicon wafer for 0.5 h under CuCl$_2$ source at 900 °C in N$_2$ gas condition. The wafer was immersed in diluted HNO$_3$ for 2 h to remove the extra element copper on the surface before further experiment. The wafer was cut to 2cm×2cm pieces and paired with MnO$_2$ cathode. The discharge current set at 0.1 mA/cm^2. The samples were washed with DI water for 6 times before dried in vacuum oven.

After electrochemical oxidation, the XPS analysis clearly shows that the ratio of –OH/O^{2-} in copper doped Si wafer is much higher than that of the pristine Si. Moreover, the presence of H$_2$O was also confirmed which may attribute to the bonding of the –OH terminated hydrophilic surface with water molecule and the adsorption of H$_2$O in the fracture.

Figure S12. Contact angle images of the (a) as prepared Cu-Si@C electrode and (b) the Cu-Si@C electrode after discharge.
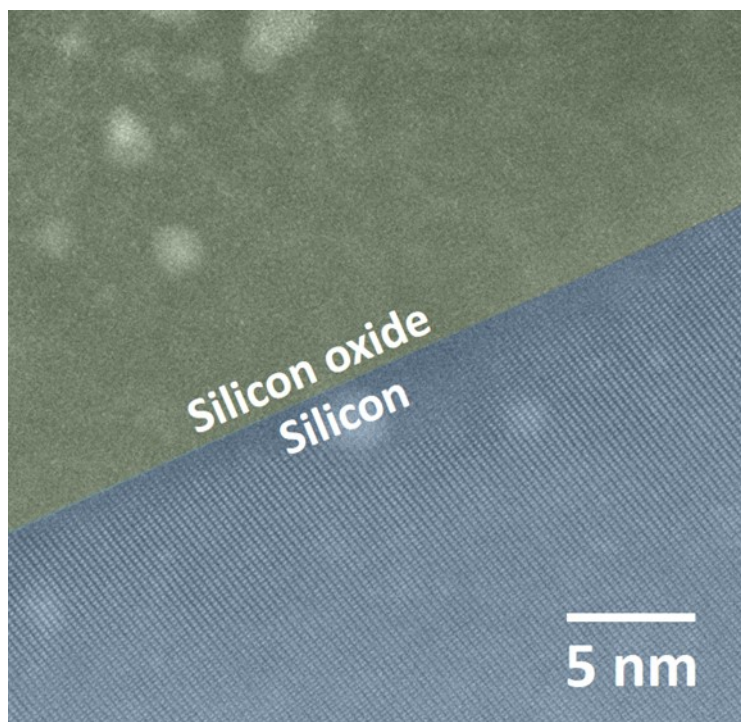
Figure S13. High-resolution STEM image of the SiO$_x$/Si interface for the Si@C after electrochemical oxidation.
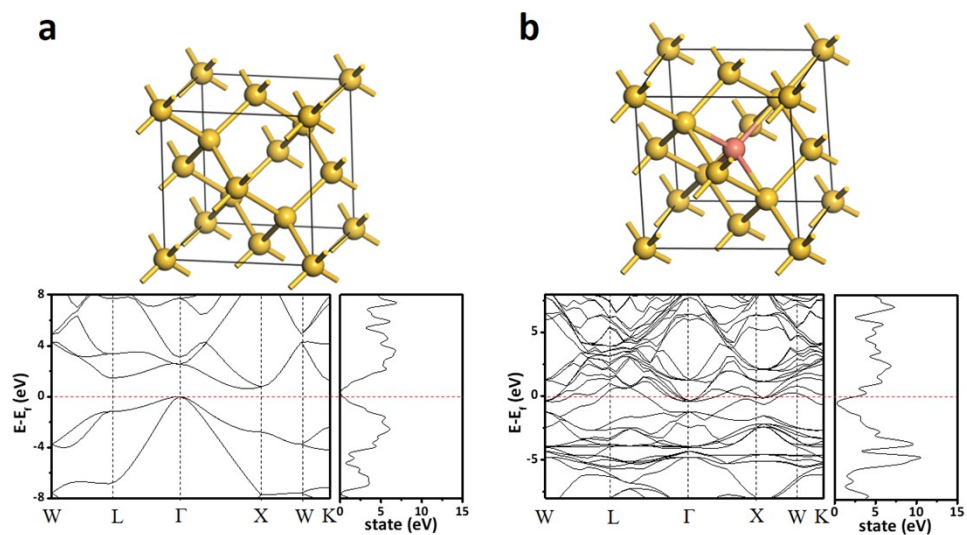
Figure S14. The DFT simulations of the band structure and density of state for (a) silicon and (b) copper doped silicon. It clearly shows that the doping of Cu atoms change silicon from semiconducting to metallic properties.
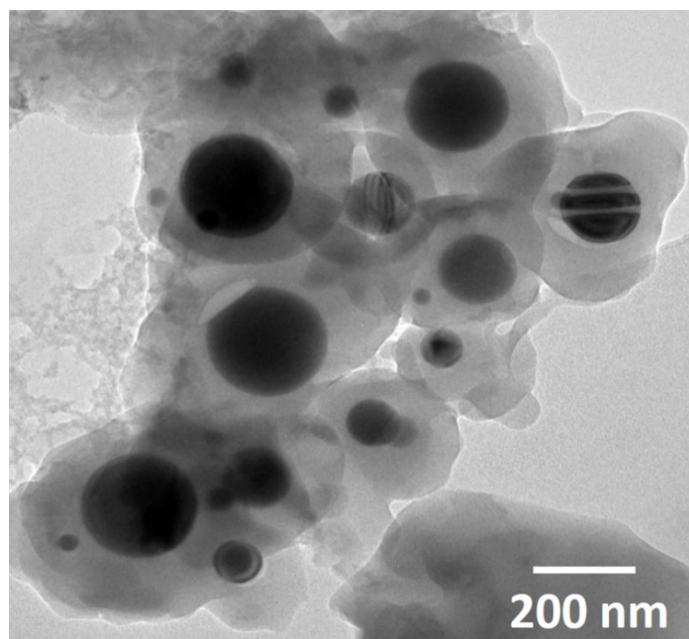
Figure S15. TEM image of the product synthesized by heat treating the $CuCl_2$ /Si (0.4g:0.2g) mixture in N_2 at 900 °C for 3 h, which clearly shows the formation of copper rich cores.
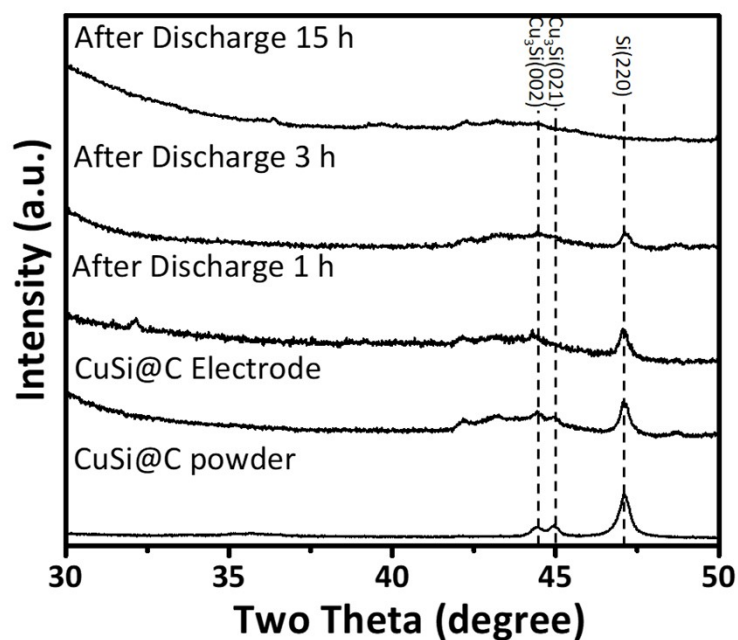
Figure S16. XRD patterns of the Cu-Si@C powder, the as prepared Cu-Si@C electrode, the electrode after discharge at 0.1 mA/cm^2 current with a MnO_2 electrode as cathode for 1h, 3 h and 15 h intervals. It clearly shows that the Cu_3Si peaks disappear after the reaction for 2 h and the silicon peak remains within the whole discharge process.
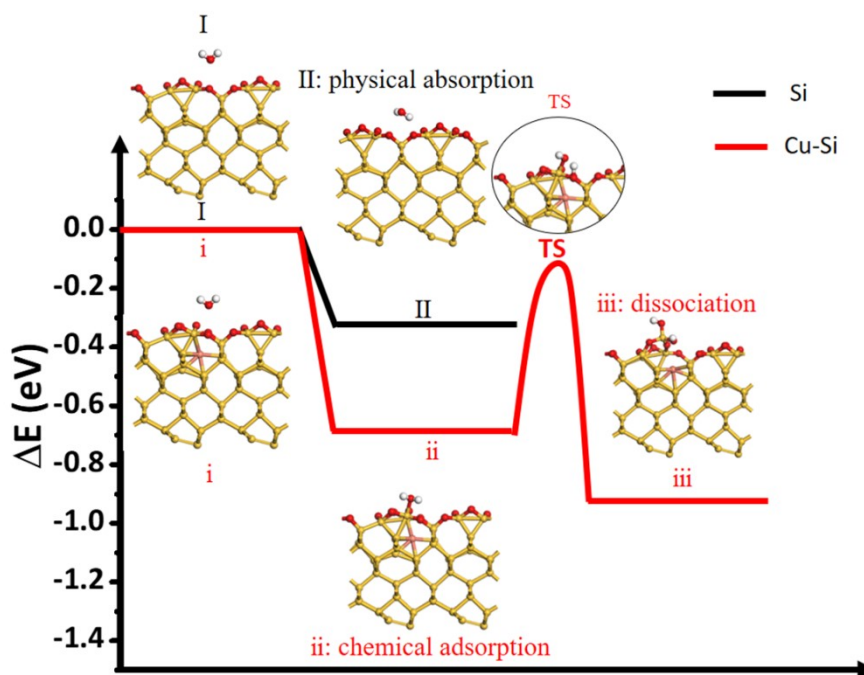
Figure S17. The DFT calculated water molecule dissociation pathways on oxidized Si and Cu-Si. For surface oxidized Si, the water molecule prefers to physically absorbed and no further dissociation takes place under normal condition. For Cu-Si, the molecule will chemically adsorb on the oxidized surface and a 0.62 eV barrier (E_a) has to be surmounted when the dissociation takes place. The water molecule dissociation induces further oxidation of the silicon. This simulation thus clearly shows that the Cu dopant can significantly reduce the activation energy for oxidation of the local silicon. The yellow atoms are Si, the white color atoms are H, the red color atoms are O and the salmon color atom is Cu.
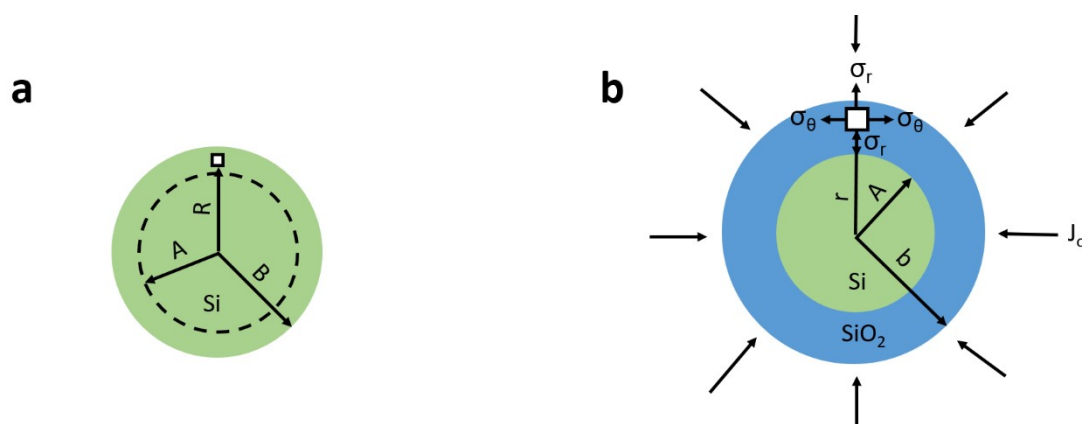
Figure S18. (**a**) The initial state of the silicon spherical particle. (**b**) In the oxidation process, the particle is partially oxidized and a field of stress is developed.
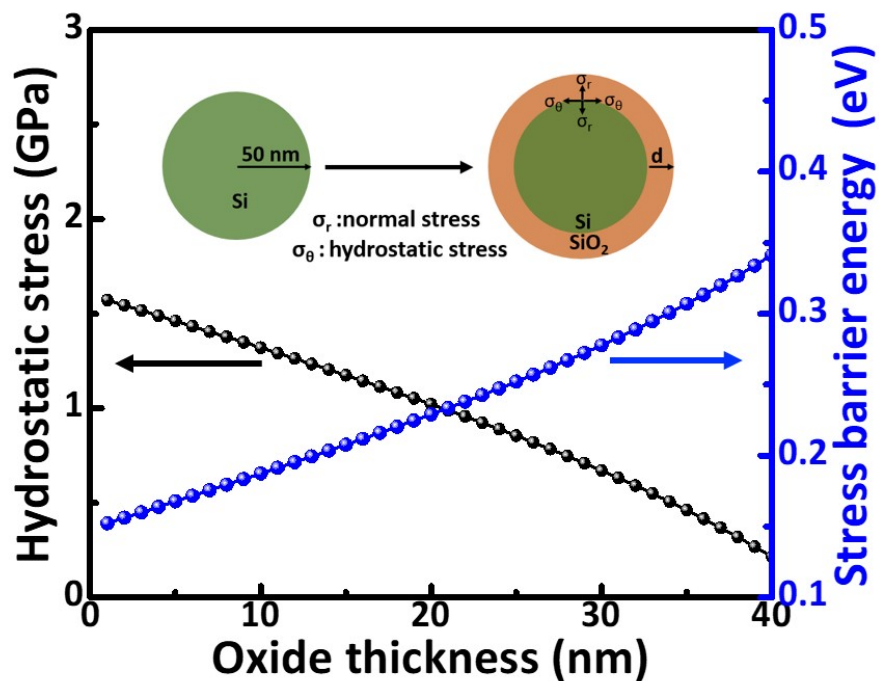
Figure S19. The contribution of the stress produced by oxidation to the driving force to retard the continuous oxidation of silicon.
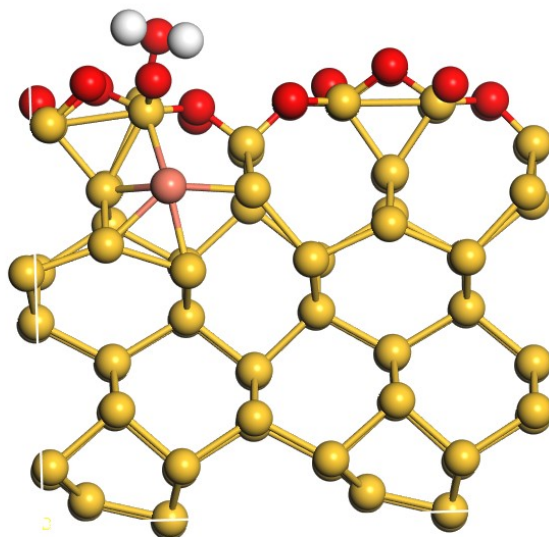
Figure S20. Schematic structure for water dissociation on $SiO_x/Si(001)$, where the yellow atoms are Si, the white color atoms are H, the red color atoms are O and the salmon color atom is Cu.
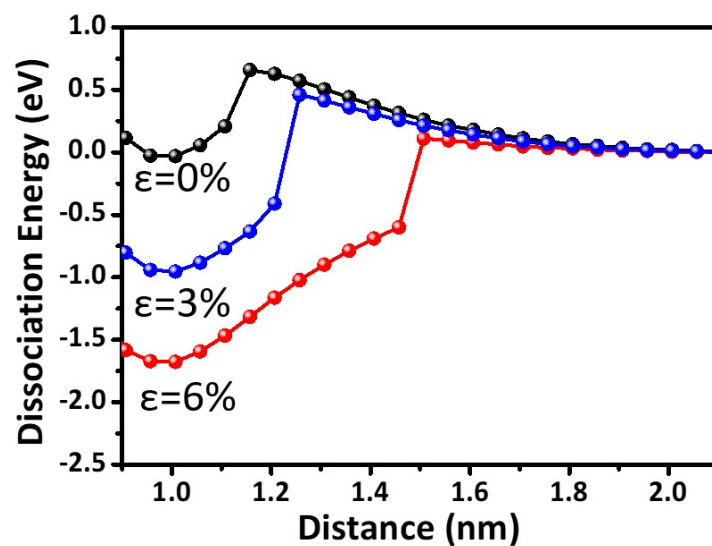
Figure S21. The simulated dissociation energy curves of water with different tensile stress applied on *x*-direction of Si based on the above SiO_x/Si structure.
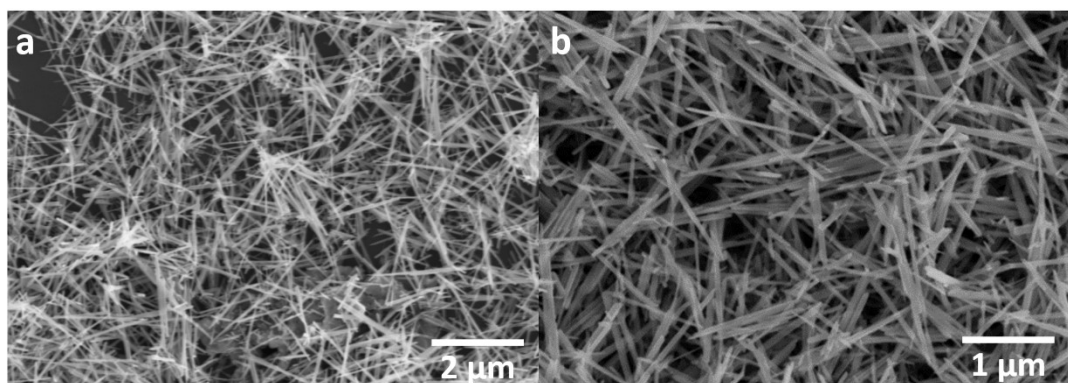
Figure S22. SEM image of (**a**) the synthesized MnO_2 nanorods, and (**b**) the MnO_2 nanorods after immersing in 1 m/kg H_2SO_4 +2 m/kg Na_2SO_4 solution for 24 h, showing its chemical stability in acid.
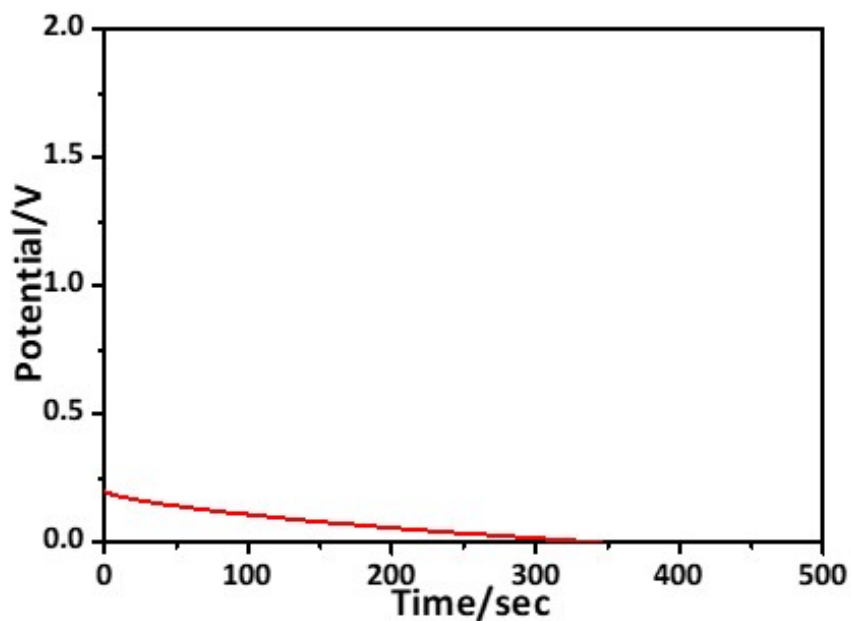
Figure S23. Galvanostatic discharge curve of one Si@C-MnO$_2$ battery. The discharge current density is 0.1 mA/cm^2. The battery only works for 300 seconds at very low output potential due to the barrier effect of the resultant SiO$_2$ during the reaction.
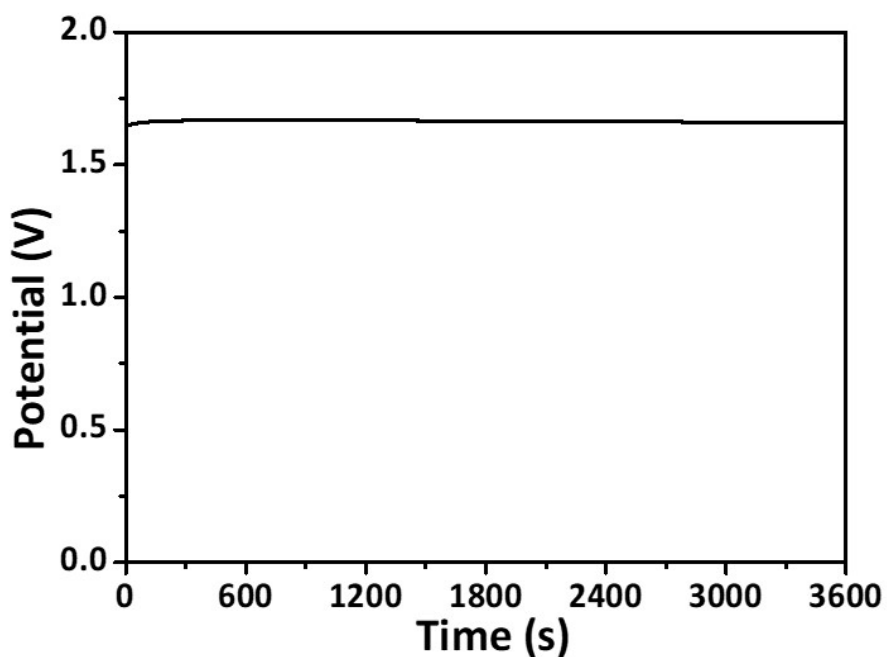
Figure S24. Open-circuit voltage of a Cu-Si@C-MnO$_2$ battery.
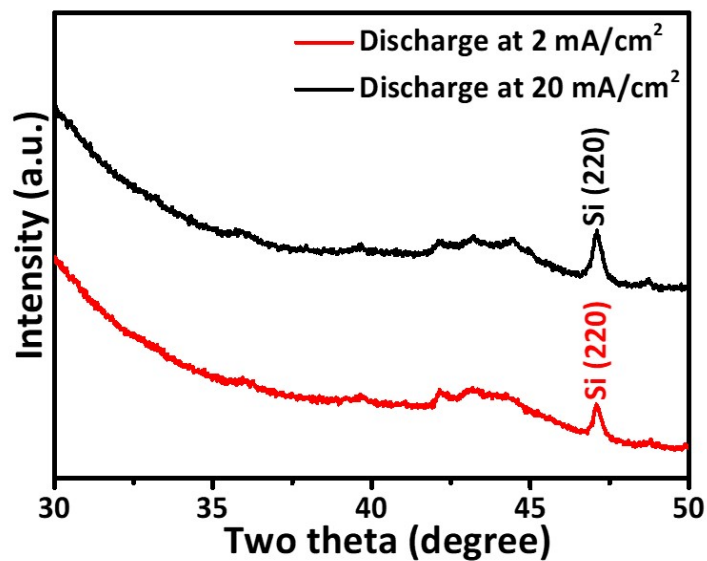
Figure S25. XRD patterns for the Cu-Si@C electrodes after discharge at 2 mA/cm^2 and 20 mA/cm^2, respectively. The crystalline Si peak was shown, confirming the presence of unreacted Si.
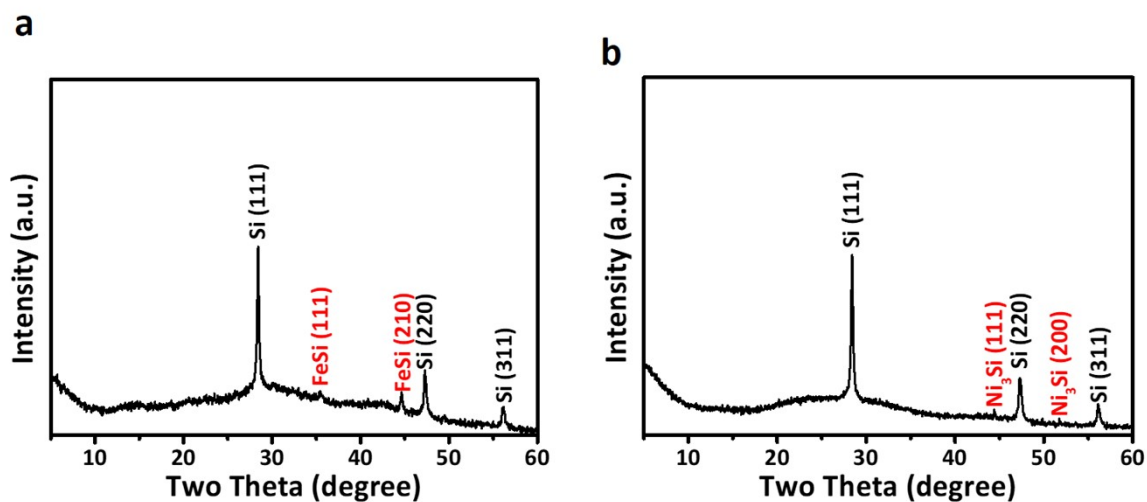
Figure S26. XRD patterns of the Fe-Si@C (a) and Ni-Si@C sample (b). The formation of FeSi and Ni$_3$Si phases was clearly shown, respectively.
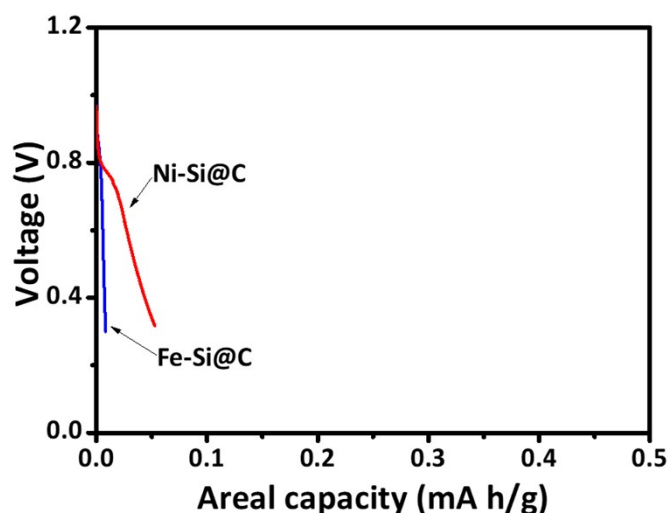
Figure S27. Areal capacities of Fe-Si@C-MnO$_2$ and Ni-Si@C-MnO$_2$ batteries under the discharge current density of 0.1 mA/cm^2. Due to their anodic properties (ref. 27), the iron and nickel silicides will also contribute to the capacities as they were formed on silicon surface. The electrochemical properties of iron and nickel silicides deposited silicon particles are currently under investigation and will be reported in the future.
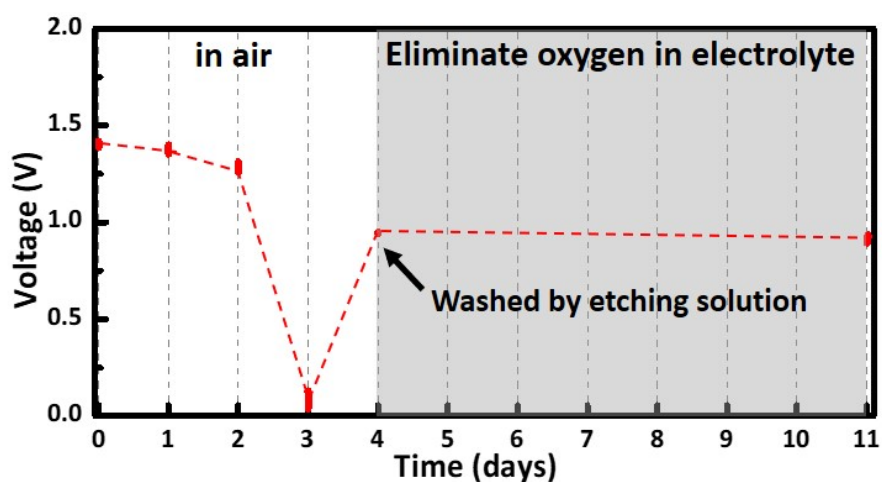
Figure S28. The discharge of one Cu-Si@C/MnO$_2$ cell under different time intervals.
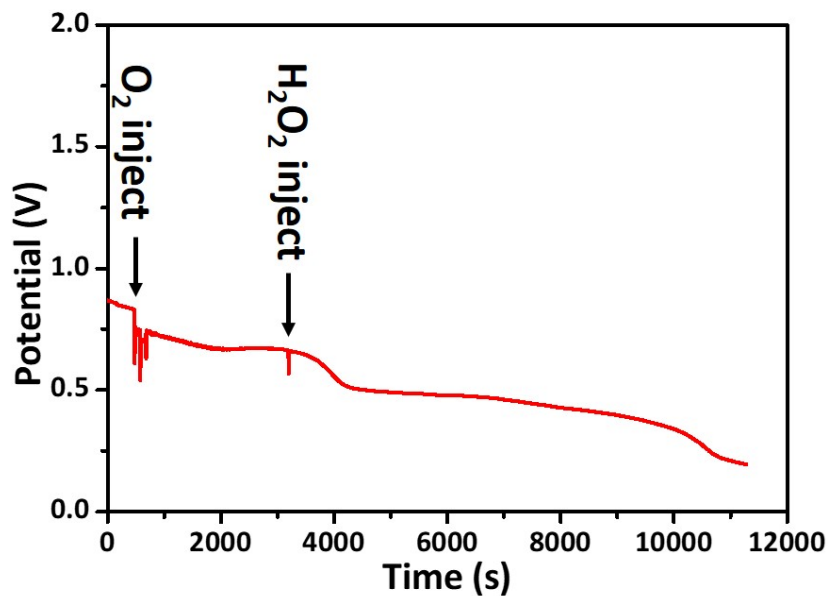
Figure S29. Discharge curve of the electrode after chemical corrosion test (Supplementary Fig.18). O_2 and H_2O_2 were injected during the process, respectively.
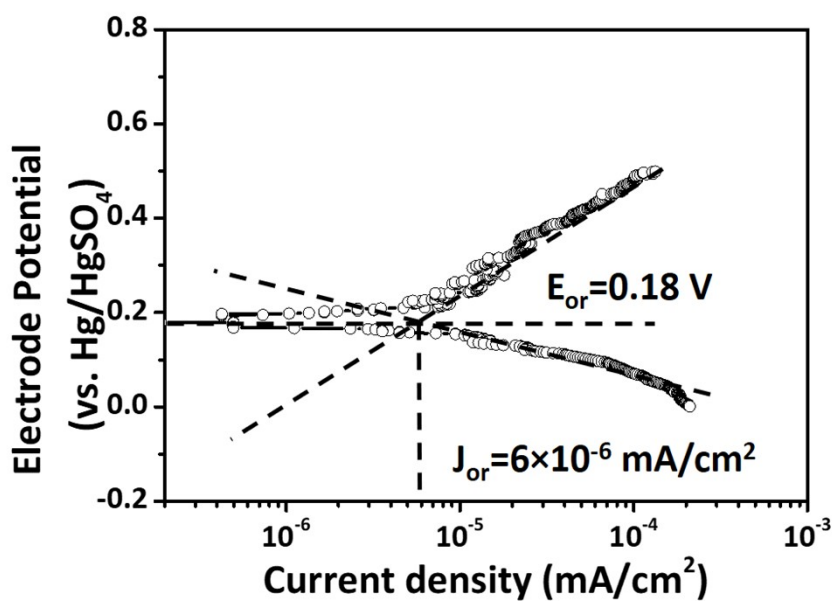
Figure S30. The potentiodynamic polarization curve of Cu-Si@C in a small potential range where the corrosion current density in acid media is calculated.
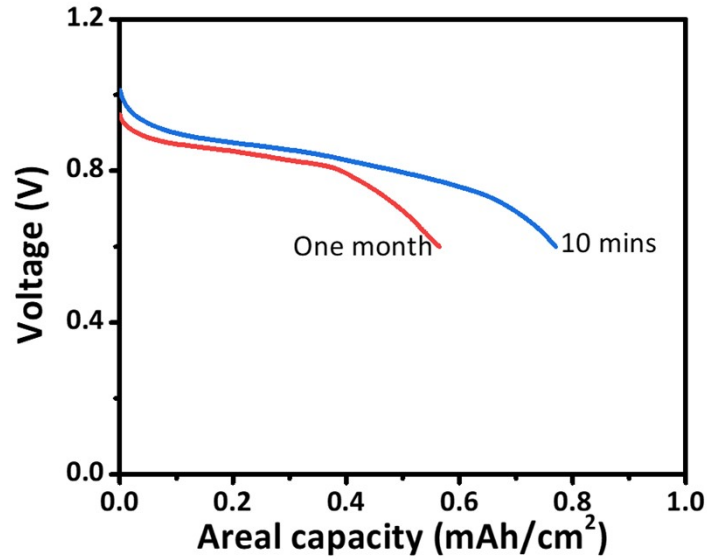
Figure S31. Discharge curves of the Cu-Si@C-MnO$_2$ battery with different rest time. The discharge current density is 1 mA/cm^2. At the cutoff voltage of 0.6 V, the battery remains 75% capacity after one month. For comparison, a Si alkaline battery with the anode having same active material loading will rapid self-discharge in 6 M KOH and the capacity becomes zero after resting less than one day.

Supplementary Table 1. Theoretical energies of various metal anode materials in the metal-air cells.

Element	n	Full cell voltage	Mass Density	Specific capacity	Capacity density	Specific Energy	Energy Density	Ref.
						excluding oxygen		
		[V]	[kg/L]	A h/kg	A h/L	[W h/kg]	[W h/L]	
Fe	2	1.28	7.87	960	7555	1229	9677	8
Zn	2	1.65	7.14	819	5848	1352	9653	9
K	1	2.48	0.89	686	610	1700	1513	10
Na	1	2.33	0.97	1166	1131	2716	2634	11
Ca	2	3.38	1.54	1338	2061	4520	6961	12
Mg	2	2.77	1.74	2206	3838	6493	11299	13
Al	3	2.71	2.70	2980	8046	8091	21837	14
Li	1	2.96	0.53	3829	2029	11238	6001	15
Si	4	2.09 (acid)	2.33	3818	8896	7979	18593	

Supplementary Table 2. Estimation of the working parameters of different primary batteries

Types	Battery reaction	Nominal voltage (V)	Capacity base on total reaction (mA h/g)	Energy of anode(W h/g)	Ref.
Zn-ion	Anode: Zn; Cathode: MnO_2; Electrolyte: $MnSO_4+ZnSO_4$ $Zn+MnO_2+2H_2O \rightarrow 2Mn(OH)_2+Zn(OH)_2$	1.5	285	0.651	17
Zn-MnO$_2$	Anode: Zn; Cathode: MnO_2; Electrolyte: NH_4Cl $Zn+2MnO_2+2NH_4Cl \rightarrow 2MnOOH+Zn(NH_3)Cl_2$	1.5	155	0.110	18
Zn-Ag$_2$O	Anode: Zn; Cathode: Ag_2O; Electrolyte: KOH $Zn+Ag_2O+H_2O \rightarrow 2Ag+Zn(OH)_2$	1.6	259	0.288	19
Zn-HgO	Anode: Zn; Cathode: HgO; Electrolyte: KOH $Zn+HgO+H_2O \rightarrow Hg+Zn(OH)_2$	1.3	179	0.255	19
Zn-air	Anode: Zn; Cathode: O_2; Electrolyte: KOH $Zn+2KOH+O_2 \rightarrow K_2Zn(OH)_4$	1.4	257	0.835	20
Li-MnO$_2$	Anode: Li; Cathode: MnO_2; Electrolyte: organic xLi$+MnO_2 \rightarrow Li_xMnO_2$	3.3	~210	~3.05	21
Li-FeS$_2$	Anode: LiAl; Cathode: FeS_2; Electrolyte: Eutectic salt $Li+FeS_2 \rightarrow Li_2S+Fe$	1.5	211	~4.2	19
Li-SOCl$_2$	Anode: Li; Cathode: $SOCl_2$; Electrolyte: $SOCl_2/LiAlCl_4$ $4Li+2SOCl_2 \rightarrow 4LiCl+SO_2+S$	3.6	403	~8.3	19
Al-S	Anode: Al; Cathode: S; Electrolyte: KOH $2Al+3S+3KOH+3H_2O \rightarrow 2Al(OH)_3+3KHS$	1.3	432	0.91	22
Al-air	Anode: Al; Cathode: O_2; Electrolyte: KOH $4Al+3O_2+6H_2O \rightarrow 4Al(OH)_3$	1.5	1031	2.5	23
Mg-AgCl	Anode: Mg; Cathode: AgCl; Electrolyte: NaCl $Mg+2AgCl \rightarrow 2Ag+MgCl_2$	1.3	172	1.8	24
Mg-MnO$_2$	Anode: Mg; Cathode: MnO_2; Electrolyte: $MgClO_4$ $Mg+2MnO_2+H_2O \rightarrow Mg(OH)_2+Mn_2O_3$	1.4	248	1.11	25
Cu-Si@C-MnO$_2$	Anode: Si; Cathode: MnO_2; Electrolyte: H_2SO_4 $Si+MnO_2 \rightarrow SiO_2+Mn^{2+}+2e$	~1.2	932	2.01	
Cu-Si@C-air	Anode: Si; Cathode: O_2; Electrolyte: H_2SO_4 $Si+O_2 \rightarrow SiO_2$	~1	2331	1.71	

Reference:

1   Clark, S. J. *et al.* First principles methods using CASTEP. *Zeitschrift Fur Kristallographie* **220**, 567-570 (2005).

2   Kejie, Z. *Mechanics of Electrodes in Lithium-Ion Batteries* phD thesis, Harvard University, (2012).

3   Wakabayashi, H. & Tomozawa, M. Diffusion of water into silica glass at low-temperature. *Journal of the American Ceramic Society* **72**, 1850-1855 (1989).

4   Lanford, W. A., Burman, C., Doremus , R. H. Diffusion of water in SiO_2 at low temperature. In: Snyder R.L., Condrate R.A., Johnson P.F. (eds) *Advances in Materials Characterization II. Materials Science Research*, vol **19**. Springer, Boston, MA (1985).

5   Morita, M., Ohmi, T., Hasegawa, E. & Teramoto, A. Native oxide-growth on silicon surface in ultrapure water and hydrogen-peroxide. *Japanese Journal of Applied Physics Part 2-Letters & Express Letters* **29**, L2392-L2394 (1990).

6   Durmus, Y. E. *et al.* Investigation of the corrosion behavior of highly As-doped crystalline Si in alkaline Si-air batteries. *Electrochimica Acta* **265**, 292-302 (2018).

7   Liang, G. *et al.* A universal principle to design reversible aqueous batteries based on deposition-dissolution mechanism. *Advanced Energy Materials* **9**, 201901838 (2019).

8   Narayanan, S. R. *et al.* Materials challenges and technical approaches for realizing inexpensive and robust iron-air batteries for large-scale energy storage. *Solid State Ionics* **216**, 105-109 (2012).

9   Li, Y. & Dai, H. Recent advances in zinc-air batteries. *Chemical Society Reviews* **43**, 5257-5275 (2014).

10   Ren, X. & Wu, Y. A Low-overpotential potassium-oxygen battery based on potassium superoxide. *Journal of the American Chemical Society* **135**, 2923-2926 (2013).

11   Das, S. K., Lau, S. & Archer, L. A. Sodium-oxygen batteries: a new class of metal-air batteries. *Journal of Materials Chemistry A* **2**, 12623-12629 (2014).

12   Reinsberg, P., Bondue, C. J. & Baltruschat, H. Calcium-oxygen batteries as a promising alternative to sodium-oxygen batteries. *Journal of Physical Chemistry C* **120**, 22179-22185 (2016).

13   Gelman, D., Shvartsev, B. & Ein-Eli, Y. Challenges and prospect of non-aqueous non-alkali (NANA) metal-air batteries. *Topics in Current Chemistry* **374**, 82 (2016).

14   Egan, D. R. *et al.* Developments in electrode materials and electrolytes for aluminium-air batteries. *Journal of Power Sources* **236**, 293-310 (2013).

15   Christensen, J. *et al.* A critical review of Li/air batteries. *Journal of the Electrochemical Society* **159**, R1-R30 (2012).

16.   Hamann, C. H., Hamnett, A., Vielstich, W. *Electrochemistry*, 2 Ed., pp:439-491, Wiley-VCH, Weinheim, **2007**.

17   Chao, D., Zhou, W., Ye, C., Zhang, H., Chen, Y., Gu, L., Davey, K., Qiao, S-Z. An electrolytic Zn-MnO_2 battery for high voltage and scalable energy storage. Angrew Chemi-International Edition, 58, 7823 (**2019**).

18.   Moulai, F., Hadjersi, T., Achour, A. The effect of zinc shape on its corrosion mitigation as an anode in aqueous Zn/MnO_2 battery. *Journal of Electroanalytical Chemistry*, 886, 115140 (**2021**).

19   Linden, D., & Reddy, T. The Handbook of Batteries (4rd Edition), McGraw-Hill Companies, Inc. **2011**.

20.   Zhang, J., Zhao, Z., Xia, Z., Dai, L. A metal-free bifunctional electrocatalyst for oxygen reduction and oxygen evolution reactions. *Nature Nanotechnology*, **10**, 444 (2015).

21.   Park, M.S., Yoon, W. Y. Characteristic of a Li/MnO_2 battery using a lithium powder anode at high-rate discharge. *Journal of Power Sources*, 114, 237 (**2003**).

22.   Peramunage, D., Licht, S. A solid sulfur cathode for aqueous batteries. *Science*, 261, 1029 (**1993**).

23. Ryu, J., Jang, H., Park, J., Yoo, Y., Park, M., Cho, J. Seed-mediated atomic-scale reconstruction of silver manganite nanoplates for oxygen reduction towards high-energy aluminum-air flow batteries. *Nature Communications*, 9, 3715 (**2018**).

24. Sammoura, F., Lee, K. B., Lin, L. Water-activated disposable and long shelf life microbatteries. *Sensors and Actuators A*. 111, 79 (**2004**).

25. Li, C., Cheng, F., Ji, W., Tao, Z., Chen, J. Magnesium microspheres and nanospheres: morphology-controlled synthesis and application in Mg/MnO_2 batteries. *Nano Research*, 2, 713 (**2009**).

26. Durmus, Y. E., Aslanbas, O., Kayser, S., Tempel, H., Hausen, F., de Gaart, L.G.J., Granwehr, J., Ein-Eli, Y., Eichel, R., Kungl, H. Long run discharge, performance and efficiency of primary silicon-air cells with alkaline electrolyte. *Electrochim. Acta*, 225, 215 (**2017**).

27 Zhang, H., Zhong, X., Shaw, J., Liu, L., Huang, Y., Duan, X. Very high energy density silicide-air primary batteries. *Energy Environ. Sci.,* 6, 2621 (2013).